

# Pushing the Limits of Extreme Weather: Constructing Extreme Heatwave Storylines with Differentiable Climate Models

Tim Whittaker<sup>1\*</sup> and Alejandro Di Luca<sup>1</sup>

<sup>1</sup>Centre Étude et simulation du climat à l'échelle régionale (ESCER),  
Département des Sciences de la Terre et de l'Atmosphère, Université du  
Québec à Montréal, Montréal, Québec, Canada.

\*Corresponding author(s). E-mail(s): [whittaker.tim@courrier.uqam.ca](mailto:whittaker.tim@courrier.uqam.ca);

## Abstract

Understanding the plausible upper bounds of extreme weather events is essential for risk assessment in a warming climate. Existing methods, based on large ensembles of physics-based models, are often computationally expensive or lack the fidelity needed to simulate rare, high-impact extremes. Here, we present a novel framework that leverages a differentiable hybrid climate model, Neural-GCM, to optimize initial conditions and generate physically consistent worst-case heatwave trajectories. Applied to the 2021 Pacific Northwest heatwave, our method produces temperature anomalies up to 3.7 °C above the most extreme member of a 75-member ensemble. These trajectories feature intensified atmospheric blocking and amplified Rossby wave patterns—hallmarks of severe heat events. Our results demonstrate that differentiable climate models can efficiently explore the upper tails of event likelihoods, providing a powerful new approach for constructing targeted storylines of extreme weather under climate change.

**Keywords:** Extreme Event Storyline, Hybrid Climate Models, Heatwaves, Automatic differentiation, Rare Event Algorithm, Optimal Control

# 1 Introduction

The 2021 Pacific Northwest (PN2021) heatwave shattered historical temperature records, culminating in Lytton, Canada’s unprecedented 49.6°C observation—a 4.6°C increase over the country’s previous record measurement [1, 2]. This event, virtually implausible under preindustrial conditions [3], exemplifies a critical challenge in climate science: determining the upper bounds of what is physically possible for different weather and climate extremes under current or future climatic conditions.

The PN2021 heatwave emerged from persistent atmospheric blocking sustained by large-scale Rossby waves that disrupted zonal flow and stalled a high-pressure system over the region [2]. These low-wavenumber waves suppressed cloud formation and prolonged subsidence, adiabatically warming near-surface air masses. Concurrent dry soil conditions, amplified by antecedent spring drought, reduced latent heat flux and increased sensible heat, further intensifying surface temperatures [2]. The interplay of the blocking persistence and land-atmosphere feedbacks culminated in the unprecedented temperature anomalies.

To systematically explore such extremes, storylines are increasingly used, representing physically consistent sequences of weather events that depict how a counterfactual extreme event might occur [4–6]. This approach enables a mechanistic exploration of how minor perturbations can lead to the amplification of extreme events. Here, we use a novel differentiable modeling framework to demonstrate that targeted initial-condition perturbations can further amplify these typical extreme trajectories, giving extreme heatwave storylines.

Identifying storylines for the most extreme weather events is a needle-in-a-haystack problem due to their inherent rarity. The traditional approach is the use of single-model initial-condition large ensembles [7–10], and more recently, so-called huge ensembles [11, 12], in which vast numbers of model runs allow the exploration of a wide range of

potential outcomes. By systematically increasing ensemble size, the chances of capturing low-probability extremes increase. However, these ensembles are computationally demanding and not very effective at sampling the full range of outcomes. In addition, due to their high computational cost, it is virtually impossible to perform such ensembles using kilometer-scale simulations, which are required to well simulate some types of weather extreme events (e.g., extreme convective precipitation).

In recent years, a number of approaches have been proposed to generate extreme event storylines [13–18]. These methods focus computing resources on specific extreme events, instead of continuous long simulations. Some approaches enhance the likelihood of simulating extreme events by constructing targeted ensembles [13, 15, 18]. [18] focus on generating an initial condition ensemble of climate model simulations of known extreme events using a method named ensemble boosting. They applied this approach to the PN2021 heatwave and by perturbing the initial conditions using numerical noise for 500 members, they found a 5-day running average of daily maximum temperature anomalies up to 2.9°C larger than the unperturbed event. Other approaches to construct storylines of extreme events use the large deviation algorithm [13, 19] where an ensemble of simulations is ran and members are periodically pruned or cloned such that an ensemble most likely to lead to an extreme event is generated. Focusing on western European heatwaves and using the large deviation algorithm, [13] generated an ensemble which has a mean 2°C anomaly compared to a control ensemble of 128 members. Other applications of the algorithm showed its ability to identify even more extreme events, with ensembles with mean anomalies of 4°C [19]. Meanwhile, [14] introduced a variational data assimilation technique, optimized with a 4D-Var inspired method to intensify past extreme tropical cyclones with minimal perturbations. This approach is closely related to the method presented here; however, we leverage automatic differentiation and computationally efficient ML-based models.

Recent advances in machine learning (ML) have led to the development of transformative tools for weather and climate modeling. Neural network architectures like GraphCast [20], Pangu-Weather [21], FourCastNet [22, 23], and FuXi [24] have demonstrated forecasting skill comparable to that of traditional numerical weather prediction systems, but at significantly reduced computational costs [25–27]. In addition to their reduced computational costs, these models by construction allow us to define optimization problems on them that can be solved through gradient-based optimizers. [25] introduced a standardized benchmark to compare the various ML models against ERA5 and the European Centre for Medium-Range Weather Forecasts’s (ECMWF) integrated forecast system (IFS). Using this benchmark, it is shown that deterministic, data-driven methods such as Pangu-Weather, GraphCast, and FuXi result in similar root-mean-square error (RMSE) in forecasting near-surface temperature, wind, and pressure up to ten days ahead. However, their forecast skill deteriorates rapidly for longer lead times, resulting in overly smoothed predictions. Using three case studies, [26] evaluated GraphCast, Pangu-Weather and FourCastNet against ERA5 reanalysis and ECMWF’s IFS for the PN2021 heatwave, the 2023 South Asian humid heatwave and a 2021 North American winter storm. They find that all data-driven models systematically underestimate the peak 2m temperature during the PN2021 heatwave, with root mean square error (RMSE) values at grid points near Vancouver, Seattle, and Portland exceeding twice the 10-day IFS error and reaching up to four times that value in Portland. During the South Asian humid heatwave, data-driven forecasts of heat index computed from 2-m air temperature and 1000-hPa relative humidity under-predicted observed peaks more strongly than IFS, particularly over Bangladesh. For the North American winter storm, data-driven forecasts of wind chill at College Station, Texas, achieved lower peak errors than IFS, with Pangu-Weather and GraphCast outperforming the operational model.

An alternative to purely data-driven approaches is the use of hybrid models, such as NeuralGCM [28], which combines a traditional dynamical core with ML components. [29] have shown NeuralGCM’s ability to hindcast the PN2021 heatwave, though due to the lack of processes (such as land-atmosphere feedbacks), the intensity of the heatwaves tends to be underestimated. Similarly to the purely data-driven models, NeuralGCM produces surface variables forecasts with skill comparable to that of the ECMWF IFS system [25]. Moreover, the use of the dynamical core both prevents the evolved fields from being overly smoothed and enhances numerical stability. These benefits allow for longer time integrations and make the model suitable for climate studies [28].

These new types of models are by their constructions differentiable through automatic differentiation [30]. The automatic differentiation property enables efficient optimization, allowing gradient-based exploration storylines in high-dimensional climate models. This is in line with many new extreme event opportunities enabled by ML models [31, 32]. Leveraging automatic differentiation, recent studies have implemented variational data assimilation techniques using neural networks, with applications ranging from toy models, such as the Lorenz 96 system [33], to reduced-order physical representations of the atmosphere [34, 35]. Additionally, [36] demonstrated that the differentiability of GraphCast allows for a more accurate reconstruction of the initial conditions that led to the PN2021 heatwave compared to using ERA5 reanalysis data. [37] explores the use of ML models and automatic differentiation to perform sensitivity analysis of the initial conditions leading to the development of cyclone Xynthia. Their findings suggest that gradients computed from the data-driven weather model at a 36-hour lead time exhibit sensitivity structures that closely resemble those generated by the adjoint of a dynamical model. In other words, the evolved perturbations from both approaches lead to similar impacts on the cyclone’s evolution.

In this study, we focus on the PN2021 heatwave event due to its well-documented synoptic drivers, including persistent blocking patterns and quasi-resonant wave amplification [2], and its prevalence in extreme event studies [1, 3, 18, 38]. We use the automatic differentiation feature of the NeuralGCM model to optimize perturbed initial conditions, and we identify trajectories where enhanced geopotential height anomalies intensify downstream near-surface temperature extremes. These storylines reveal heatwave intensity increases of  $3.7^{\circ}\text{C}$  beyond the extreme temperatures obtained from a 75-member ensemble run using NeuralGCM for the event, analogous to the ensemble boosting approach [18]. Our results demonstrate the potential of differentiable hybrid models for investigating worst-case scenarios, offering a computationally efficient alternative to traditional, computationally expensive, large ensembles.

## 2 Results

### 2.1 NeuralGCM temperature evaluation

We first evaluate the ability of the NeuralGCM model to simulate a temperature climate to ERA5. Figure 1a) presents the 6-hourly temperature distribution for a NeuralGCM simulation and the ERA5 data over the 1981-2020 40-year period, averaged within the domain of interest (highlighted in the blue box in Fig. 2). The NeuralGCM simulation closely approximates the ERA5 distribution, demonstrating its ability to reproduce key statistical characteristics of the temperature distribution in this region. We highlight the 95th and 99th percentile values for both the model and ERA5. We note that the model has slightly colder hot extremes than ERA5.

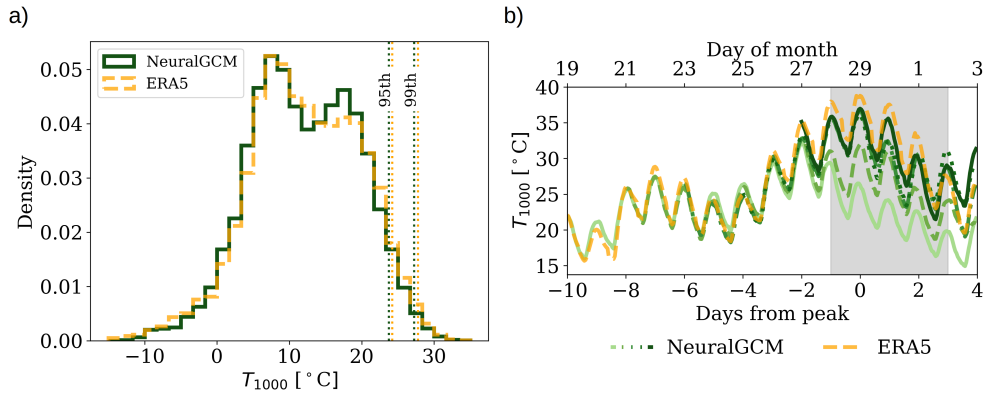


**Fig. 1** (a) Histograms of 6-hourly temperature values from a 40-year NeuralGCM simulation (green) and from ERA5 (orange) reanalysis over the study domain outlined in Figure 4. Dashed line indicates the 95th and 99th percentiles. (b) Time series of temperature forecasts at 1000hPa from NeuralGCM with 10-, 6-, 4-, and 2-day lead times (green colored lines) compared with ERA5 reanalysis data (orange line) for the PN2021 heatwave. Grey area highlights the targeted time range for the optimization process.

Next the ability of the NeuralGCM model to forecast the PN2021 heatwave against the ERA5 reanalysis data is evaluated. Figure 1b) shows NeuralGCM forecasted surface temperatures during the PN2021 heatwave for five lead times ranging from 10 to 2 days. At a 10-day lead time, the NeuralGCM predictions follow closely the ERA5 data until about day 8, where they deviate leading to a lack of heatwave and extreme temperatures. At an 8-day lead time, the simulation substantially enhances temperature during the heatwave period but still shows large underestimations of peaks intensities, with differences of about 6 °C. At 2-, 4-, and 6-day lead times, the NeuralGCM model captures well the general pattern of temperature variations shown by ERA5, including the occurrence of very high temperatures during the heatwave event. However, most forecasts underestimate the peak intensity compared to ERA5 by a few degrees Celsius, particularly during the days after the peak intensity.

## 2.2 Optimizing extreme temperatures

We optimize the initial conditions of the NeuralGCM model starting from June 21st, 2021 (corresponding to a lead time of 8 days to the peak of PN2021; see Sect. 5 for details) and run the simulation forward for 11 days. An 8-day lead time strikes a balance between two requirements: keeping the event within the model’s predictable window and allowing enough time for small perturbations to develop. The optimization is performed using gradient descent over 75 steps to solve eq. 3, targeting the last 5-days of the event (see grey shaded area in Fig. 1). The full set of parameters used in the optimization is provided in Tab. 1. Figure 2 shows the differences in 500-hPa geopotential height ( $\phi_{500}$ ; top row) and the 1000-hPa temperature ( $T_{1000}$ ; bottom row) between the optimized (OPT) and control (CTL) trajectories. In addition, the  $\phi_{500}$  and  $T_{1000}$  of the optimized simulation are shown in dark contour lines. The early day conditions (T-6 day) show minimal differences, with anomalies amplifying progressively as we get closer to the peak day. Positive and negative differences in  $\phi_{500}$  are generally observed in association with ridges and troughs, respectively, indicating that the optimized simulation amplifies the hemispheric wave amplitudes. Specifically, over the targeted region, there is a clear increase in  $\phi_{500}$  and  $T_{1000}$ , with the largest increases centered over the targeted region.

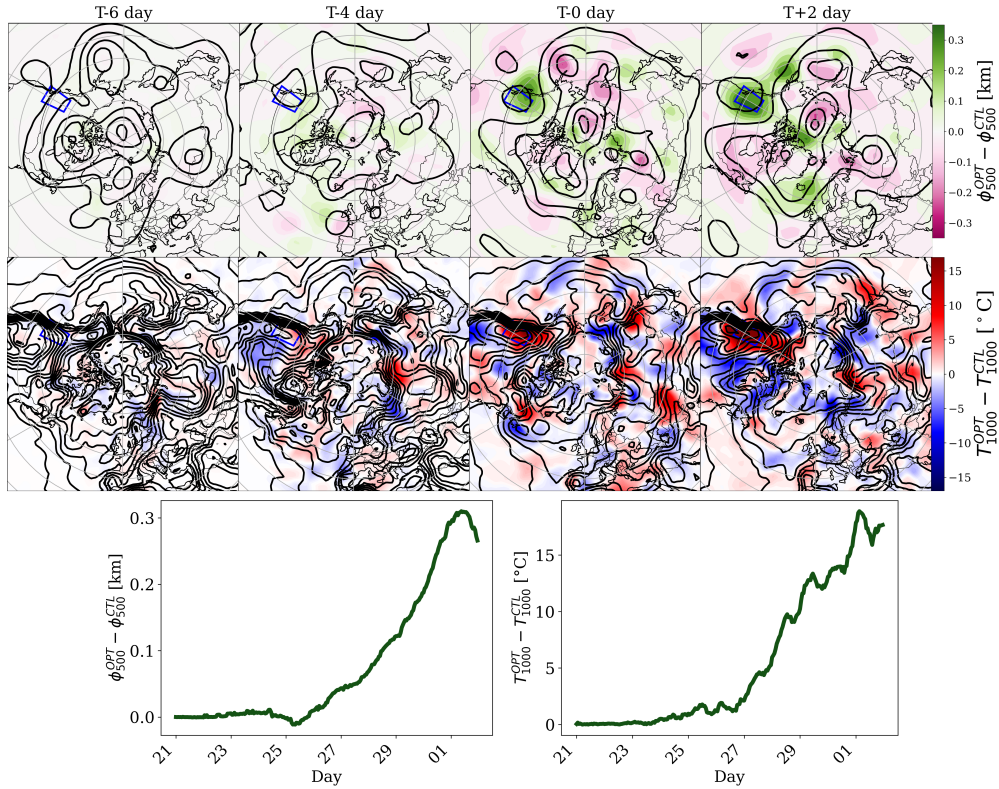


**Fig. 2** Top row: Evolution of the difference in 500-hPa geopotential height ( $\Delta Z$ , in km) between the optimized simulation and the control run. Black contours (optimized run) outline the amplified Rossby wave pattern, with deeper troughs and higher ridges compared to the control. Middle row: The difference in 1000-hPa temperature ( $^{\circ}\text{C}$ ) between the optimized and control simulations. Bottom row: The difference between the 500-hPa geopotential height and 1000-hPa temperature averaged over the target domain.

We examine the 500-hPa geopotential height along a fixed latitude (latitude =  $57.2^{\circ}$ ) in Fig. 3. The wave patterns produced by the optimized simulation are compared to those from the control simulation, along with their respective spectral characteristics during the last three days of the event. Notably, the geopotential height near the heatwave region is significantly higher in the optimized simulation compared to

the control one. Both the control and optimized simulations show signs of a persistent wavenumber three wave. In the spectral amplitude, the largest differences in spectral amplitude occur for wavenumbers 2–5, which are typically associated with heatwave events. Specifically, the largest differences are observed at wavenumber 3, followed by 2 and 4, where the optimized simulation exhibits greater power than the control simulation. While some differences are also present at higher wavenumbers, their magnitude is substantially smaller.

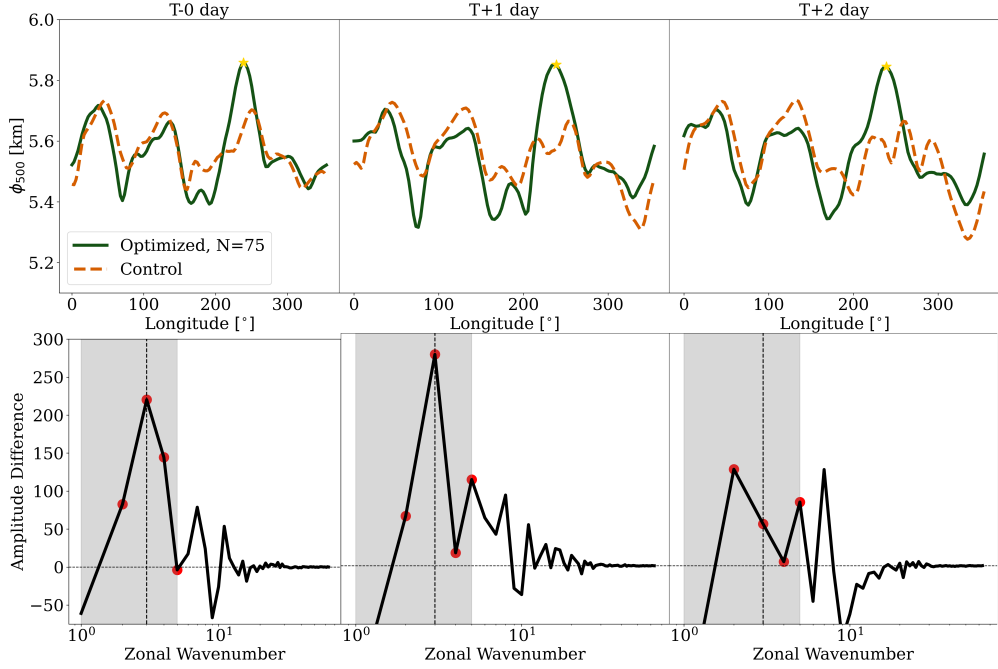


**Fig. 3** Top row: cross section of 500 hPa geopotential along a fixed latitude. Bottom row: the amplitude difference of the Fourier spectrum, including wavenumbers 1–5 highlighted in grey. Red dots highlight wavenumbers 2–5.

The optimization process relies on gradient descent (see Sect. 5 for details), which requires choosing the number of the number of gradient descent steps. Figure 4 shows

hourly time series of  $T_{1000}$  (Figure 4a) and  $\phi_{500}$  (Figure 4c) for two optimized trajectories with  $N = 50$  and  $N = 75$  steps, alongside a 75-member ensemble and its mean, all initialized 8 days before the peak of the event. The ensemble was obtained using the stochastic implementation of NeuralGCM (see Sect. 5 for details). Notably, the  $T_{1000}$  time series (Fig. 4 a) reveals that both optimized trajectories attain values beyond the range exhibited by any individual ensemble member. In other words, the proposed method allows to find extreme temperature values that are more extreme than those found using a 75-member ensemble using only 50 iterations (a 33% reduction in computational cost). Specifically, the trajectory from 50 steps reaches a peak temperature of  $37.0^{\circ}\text{C}$ , while the trajectory after 75 steps attains  $38.9^{\circ}\text{C}$ . Compared to the mean of the ensemble, we reach anomalies of  $14.0^{\circ}\text{C}$ . For the 500-hPa geopotential height (Fig. 4c), both optimized trajectories show similarly elevated values, once again exceeding the range spanned by the 75-member ensemble. Importantly, the trajectory from the 75-step optimized run maintains a more sustained increase of the 500-hPa geopotential height compared to that from the 50-step run. The measured intensity (Fig. 4e) and length of the event (Fig. 4f) are increased in both optimized runs compared to the ensemble mean. Both optimized runs produce a 6-day-long heat-wave event, differing only in intensity, with the 75-step run having a  $1.0^{\circ}\text{C}$  higher intensity than the 50-step run. Notably, both optimized solutions exceed the intensities spanned within the 75-members ensemble. Figure 4b,d present the temperature and geopotential fields from the 75-iteration run. The temperature pattern features a maximum over the targeted region, albeit slightly to the south, while the 500 hPa geopotential height field exhibits an anticyclone directly overhead.

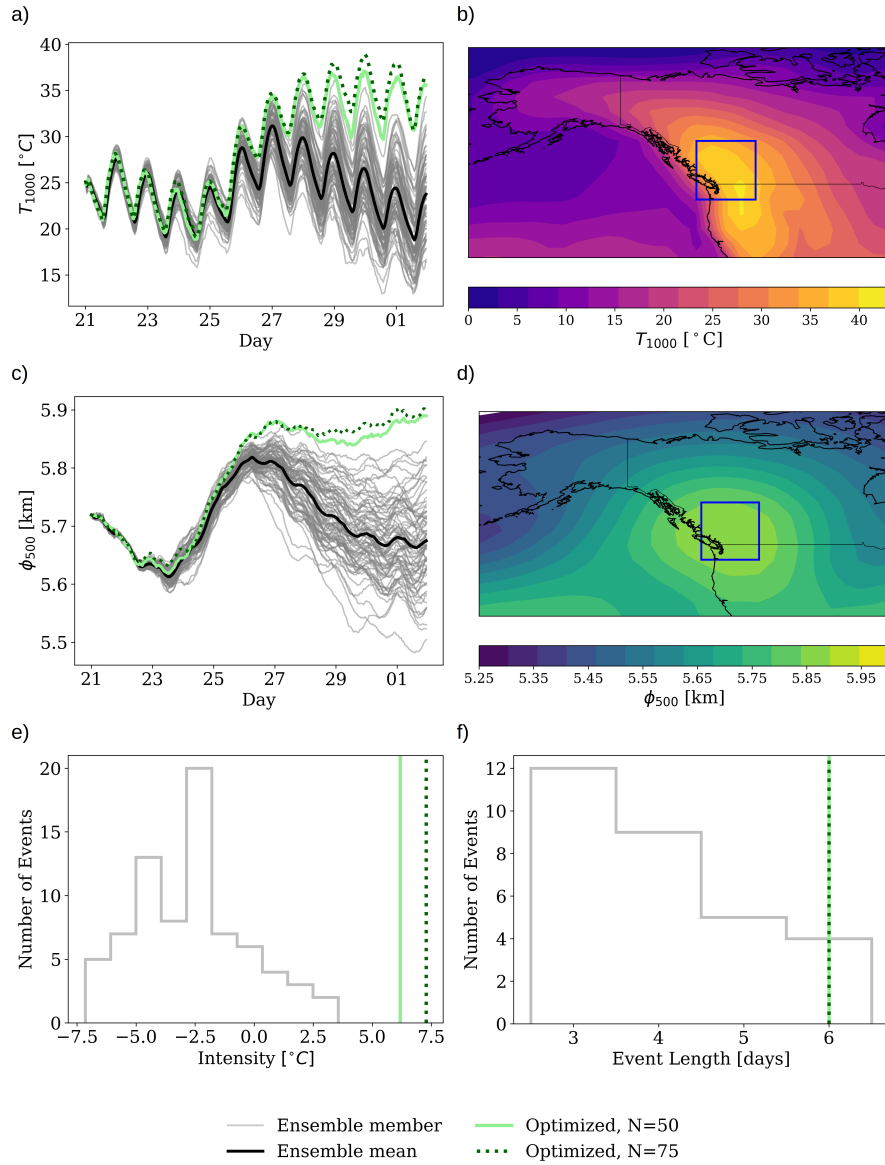


**Fig. 4** (a) Time series of 1000-hPa temperature for two optimized trajectories (50 and 75 steps) and a 75-member ensemble with its mean. (b) Spatial map of average temperature anomalies from the 75-step run. (c) Time series of 500-hPa geopotential height for the same set of simulations. (d) Spatial map of 500-hPa geopotential height anomalies during the event period. (e, f) Time series of heatwave intensity (defined by Eq. 4) and duration for the ensemble and optimized cases.

### 3 Discussion

Our findings demonstrate that differentiable climate models, exemplified by NeuralGCM, offer a powerful tool for constructing extreme heatwave storylines through gradient-based optimization of initial conditions. By perturbing initial conditions, we identified alternative trajectories with slightly different synoptic-scale conditions that amplify the PN2021 heatwave intensity by  $3.7^{\circ}\text{C}$  according to NeuralGCM. These results align with prior studies linking extreme heat to persistent blocking patterns [2, 39]. Specifically, the optimized geopotential height anomalies and spectrum reflect enhanced blocking dynamics with an amplification of wavenumbers 1-5.

While NeuralGCM resolves large-scale dynamics, its omission of land-atmosphere feedbacks (e.g., soil moisture [29]) likely results in a conservative estimate of heatwave amplification. For instance, soil moisture–temperature coupling is known to cause stronger heatwave persistence (e.g., [1, 8]), implying that the model might underestimate extremes when such feedbacks are neglected. Additionally, the model’s coarse horizontal resolution ( $2.8^{\circ}$ ) introduces biases in capturing localized extreme conditions associated with the PN2021 event. As show in the Appendix B, the use of finer grids ( $1.4^{\circ}$ ) allows for more accurate estimates of the extreme temperatures of the event although the main dynamical changes remain similar to the coarse resolution. In addition, while we have chosen to use NeuralGCM for this study, the method could be applied to any model which had automatic differentiation implemented. This includes all existing purely data-driven models, including GraphCast, Pangu-weather, FourCastNet, and FuXi. While data-driven models could provide faster predictions at higher resolution, their dual-initial-condition requirement introduces ambiguity about finding optimal initial conditions. For instance, [36] optimized both inputs for GraphCast to reconstruct the 2021 heatwave, but this approach demands simultaneous perturbation of two distinct states. Validation against models like Pangu demonstrated

that results remained consistent despite this added complexity, suggesting robustness in the dual-input framework. However, NeuralGCM’s hybrid design simplifies the workflow by requiring only a single initial condition. In addition, [40] show that data-driven forecast models tend to poorly represent small perturbations, often filtering them out, which could impact the method. The extent to which this affects hybrid models, which has a dynamical core, such as NeuralGCM remains unclear.

The optimization process involves making several decisions and setting specific parameters. While we do not present the results here, we have explored a limited subset of the broader hyperparameter space—specifically, the learning rate ( $\alpha$ ) and the loss function parameters  $(\beta, \vec{\lambda})$ . We found that, for the loss function parameters defined in Sect. 5, a large learning rate induces instability, causing substantial perturbations without a corresponding increase in temperature and in some cases, triggering numerical instabilities that caused the simulation to fail. To ensure stability,  $\alpha$  must be on the order of  $10^{-9}$  or smaller. This stability condition varies in a nonlinear and nontrivial manner with changes in  $\vec{\lambda}$ , and a thorough exploration of the hyperparameter space lies beyond the scope of this study. Fine-tuning the parameters might allow for improved efficiency in computational cost, where a more extreme solution is found with a reduced number of steps.

To evaluate the robustness and physical realism of the NeuralGCM-optimized initial conditions, these perturbations should be tested in a conventional numerical weather prediction model (e.g., Environment and Climate Change Canada’s model [41]). Such cross-model validation would reveal the universality of the results and help isolate NeuralGCM-specific biases. Additionally, running these scenarios in a fully physical model would explicitly account for land–atmosphere interactions and feedbacks, and assess whether the extreme trajectories persist under more detailed dynamics and physics.

The computational efficiency of the ML and hybrid models coupled with their differentiable properties, opens avenues for exploring extreme events—from heatwaves to precipitation extremes and compound disasters. For example, a similar optimization problem could be formulated for StormCast [42] to allow us to search for extreme precipitation events in an emulated regional climate model. One could also formulate the loss function such that the large deviation theory rate function is minimized, leading to “typical” trajectories of extremes [43, 44]. We could also envision loss functions with hard constraints on the perturbation which impose conservation laws as opposed to simply imposing small perturbations.

## 4 Conclusions

We introduce a differentiable-storyline framework that leverages automatic differentiation in hybrid climate models to directly optimize initial conditions and generate physically coherent extreme-heatwave trajectories at a fraction of the computational cost of traditional ensemble methods. When applied to the PN2021 heatwave, our approach produces intensifications of nearly  $3.7^{\circ}\text{C}$  by isolating high-impact circulation patterns, specifically enhanced blocking and Rossby-wave, demonstrating both its dynamical fidelity and efficiency. While this proof-of-concept focuses on NeuralGCM and a single case study, the optimization paradigm is agnostic to model architecture and event type, offering a transformative tool for rapid, process-based risk assessment of diverse climate extremes in a warming world.

## 5 Methods

### 5.1 Optimization Problem

The optimization process is framed through a continuous-time dynamical system. For conceptual clarity, we describe the problem using an ordinary differential equation

system:

$$\dot{\vec{x}} = b(\vec{x}(t, \vec{x}_0)), \quad (1)$$

with  $b$  representing some nonlinear operator,  $t$  the time and  $\vec{x}_0$  some initial state. The solution is given by  $\vec{X}(t) = S_t \vec{x}_0$  where  $S_t$  is the evolution operator up to time  $t$ . The core aim of the optimization problem is to identify the initial conditions  $\vec{x}_0$  that drive the dynamical system toward an extreme desired state, represented by a target observable  $\mathcal{O}(\vec{X}(t))$  at a future time  $T$ . Given a baseline initial state  $\vec{x}_0^0$ , we define a perturbation  $\Delta \vec{x}_0^i = \vec{x}_0^i - \vec{x}_0^0$ . The optimization problem is formulated as minimizing a loss function:

$$\mathcal{L}(\vec{X}(t), \Delta \vec{x}_0) = F(\mathcal{O}(\vec{X}(t))) + \vec{\lambda} \cdot \Delta \vec{x}_0^2, \quad (2)$$

where the first term is designed to favor more extreme values of the observable by applying a cost function  $F$  to the outcome  $\mathcal{O}(\vec{X}(t))$ , and the second term, scaled by the regularization parameter  $\vec{\lambda}$ , penalizes the magnitude of the initial perturbation  $\Delta \vec{x}_0^i$ . This formulation balances the competing objectives of inducing a rare event and keeping the initial perturbation sufficiently small.

In particular, we pick our observable to be the temperature over a domain  $\mathcal{D}$  and over a period of time  $\tau$  at the 1000-hPa pressure level of the model. Multiple functions can be considered to achieve this, but our main results use :

$$\mathcal{L}(T_{1000}, \Delta x_0) = \underbrace{\beta \frac{T_{\text{ref}}}{\tau |\mathcal{D}|} \int_0^\tau \int_{\mathcal{D}} T_{1000}(x, t) dx dt}_{\text{Heatwave intensity term}} + \underbrace{\sum_i \lambda_i \frac{(\Delta x_{0,i})^2}{(\Delta x_{\text{ref},i})^2}}_{\text{Perturbation penalty term}} \quad (3)$$

where  $\mathcal{D}$  corresponds to the region shown in Fig. 4, and  $\tau$  is set to 5 days. The terms in the objective function are normalized by their initial means, with  $T_{\text{ref}}$  representing a characteristic temperature scale and  $\Delta x_{i,\text{ref}}$  denoting a reference perturbation scale for each component  $i$ . The normalization scale for each perturbed variable,  $\Delta x_{\text{ref},i}$ , is

defined as the absolute mean of each respective initial field. This ensures each terms is of a similar magnitudes.

## 5.2 Numerical Implementation

To simulate the dynamics and evaluate the loss function, we use the NeuralGCM model [28] with a horizontal grid spacings of  $2.8^\circ$ . NeuralGCM has been implemented in JAX [45] and supports automatic differentiation. This enables the computation of gradients with respect to both initial conditions and internal system parameters, facilitating backpropagation through the physical dynamics and neural network components. In this work, we compute gradients only with respect to the initial variables involved in the dynamical core of NeuralGCM, keeping all other parameters fixed. The loss, as defined in Eq. 3, is minimized using gradient descent, specifically with the Adam optimizer from Optax [46]. The optimal perturbations are applied on the spherical harmonic coefficients representation of the variables. We choose NeuralGCM over other possible models because, it has demonstrated competitive forecast skill for temperatures up to 10-day lead times, contains a dynamical core and relies on a single initial condition.

Although the model runs efficiently on a single GPU with relatively low memory requirements, gradient computation demands substantial memory, scaling rapidly with the number of time steps. To address this, we employ gradient checkpointing and chunking strategies to manage memory usage. These techniques store only essential intermediate values during the forward pass, recomputing them during the backward pass to reduce memory overhead [28]. The optimization scheme on the  $2.8^\circ$  model runs on a 16GB A4000 Nvidia GPU, whereas the  $1.4^\circ$  model necessitates a 40GB A100 Nvidia GPU.

We investigate extreme events by perturbing the initial conditions primarily around PN2021 using data from the ERA5 reanalysis dataset [47]. We conducted two simulations; their configurations—including the learning rate ( $\alpha$ ), loss-function weights ( $\beta, \vec{\lambda}$ ), forecast lead times, initialization dates, and number of steps are detailed in Table 1.

$\alpha$	$\beta$	$\lambda_T$	$\lambda_{SP}$	$\lambda_\delta$	$\lambda_\zeta$	$\lambda_{SH}$	$\lambda_{SCIWC}$	$\lambda_{SCLWC}$	Initial Date	$\tau$	Total integration time	steps
$10^{-9}$	20	200	20	2000	2000	200	20	20	June 21st 2021	5 days	11 days	50
$10^{-9}$	10	100	10	1000	1000	100	10	10	June 21st 2021	5 days	11 days	75

**Table 1** Parameters used during optimization process.

The optimized simulations are compared to an ensemble run of the event using the stochastic version of NeuralGCM. This ensemble consists of 75 members. Unlike our approach, which perturbs the initial conditions (inputs to the model), the stochastic model introduces perturbations within the learned physics module. As a result, the perturbations are effectively introduced one time step apart. Additionally, our method perturbs surface pressure, which is not perturbed in the stochastic model. More details about the stochastic model can be found in [28].

### 5.3 Heatwave Intensity

We define a heatwave event as a period during which the daily temperature exceeds the 99th percentile threshold for consecutive days [48]. The length of the event is given by the number of consecutive days the temperature remains above this threshold. The intensity of the heatwave is measured by the average exceedance of the temperature above the threshold over the duration of the event. Specifically, if  $L$  denotes the length of the event,  $T_i$  the mean temperature timeseries over a region, and  $T_{\text{thresh}}$  the 99th percentile threshold, then the intensity  $I$  is defined as

$$I = \frac{1}{L} \sum_{i=1}^L (T_i - T_{\text{thresh}}). \quad (4)$$

In our analysis we compare the intensity,  $I$ , of the heatwaves from the optimized runs with those from the ensemble runs over the targeted five days of the optimization process.

## 5.4 Perturbations

Table 2 presents the maximum perturbations applied to the initial conditions, alongside the range of values sampled in the ensemble simulation. The ensemble perturbation methodology, described in Sect. 5, does not include perturbations to surface pressure. The range is computed by finding the max perturbation of all the ensemble members with respect to the mean. Overall, the applied perturbations during optimization remain within or below the variability represented in the stochastic ensemble.

Quantity	Max Perturbation (N = 50)	Max Perturbation (N = 75)	Range of Perturbations Ensemble Run
Surface Pressure (Pa)	0.69	0.47	0.0
Specific Humidity	$2.34 \times 10^{-3}$	$1.11 \times 10^{-3}$	$3.20 \times 10^{-3}$
Specific Cloud Ice Water Content (kg kg <sup>-1</sup> )	$7.61 \times 10^{-6}$	$5.19 \times 10^{-6}$	$4.35 \times 10^{-5}$
Specific Cloud Liquid Water Content (kg kg <sup>-1</sup> )	$1.50 \times 10^{-5}$	$2.42 \times 10^{-5}$	$7.61 \times 10^{-5}$
Temperature (K)	4.83	4.99	7.60
U-component of windspeed (m s <sup>-1</sup> )	8.37	5.59	12.70
V-component of windspeed (m s <sup>-1</sup> )	4.77	4.12	7.94

**Table 2** Maximum perturbations for different run sizes compared to the range of perturbations applied on the ensemble run by the stochastic model.

**Acknowledgments.** T.W. would like to thank Robin Noyelle, and Eric Vandeneijnden for discussions which lead to this project. T.W. would like to thank Seth Taylor and Tangui Picart for discussions and comments on the draft. The authors would like to thank Frédéric Toupin, Katja Winger, and Francois Roberge for maintaining a user-friendly local computing facility. This research was enabled in part by support provided by Calcul Québec (calculquebec.ca) and the Digital Research Alliance of Canada (alliancecan.ca).

## Declarations

- Funding: NSERC CGS D - 588387 - 2024.
- Data availability: All data generated using the code and ERA5 data used in this study is openly available from the Copernicus Data Store (<https://doi.org/10.24381/cds.143582cf>) [47].
- Code availability: <https://github.com/timwhittaker/ExtremeStorylines>

## Appendix A Extra Figures

In addition, we show the optimized trajectories Fig. A1 for the other model outputs. We can see that the optimized trajectories show moderately higher values of surface pressure, lower values of specific humidity, higher values of eastern winds and higher values of southern winds compared to the non-optimized ensemble.

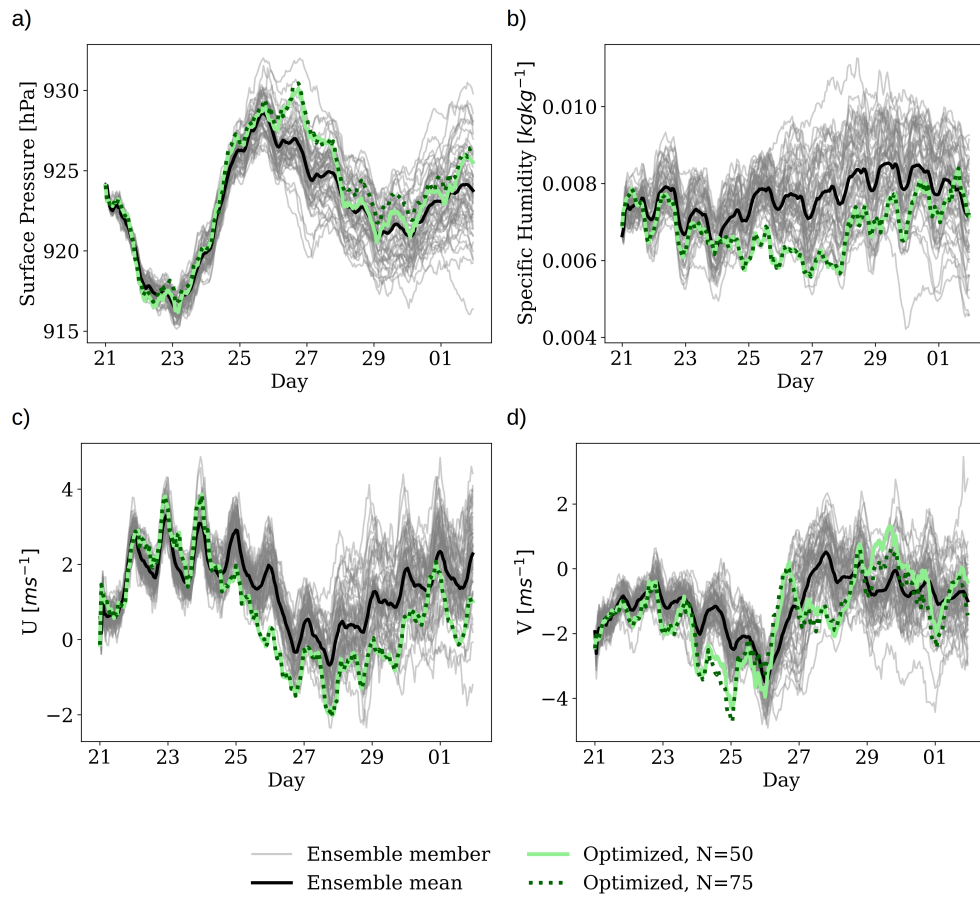


**Fig. A1** (a) Time series of surface pressure; (b) Time series of specific humidity; (c) Time series of the u-component of wind; (d) Time series of the v-component of wind. Data from the optimized trajectory are shown alongside ensemble members and ensemble mean.



## Appendix B 1.4° results

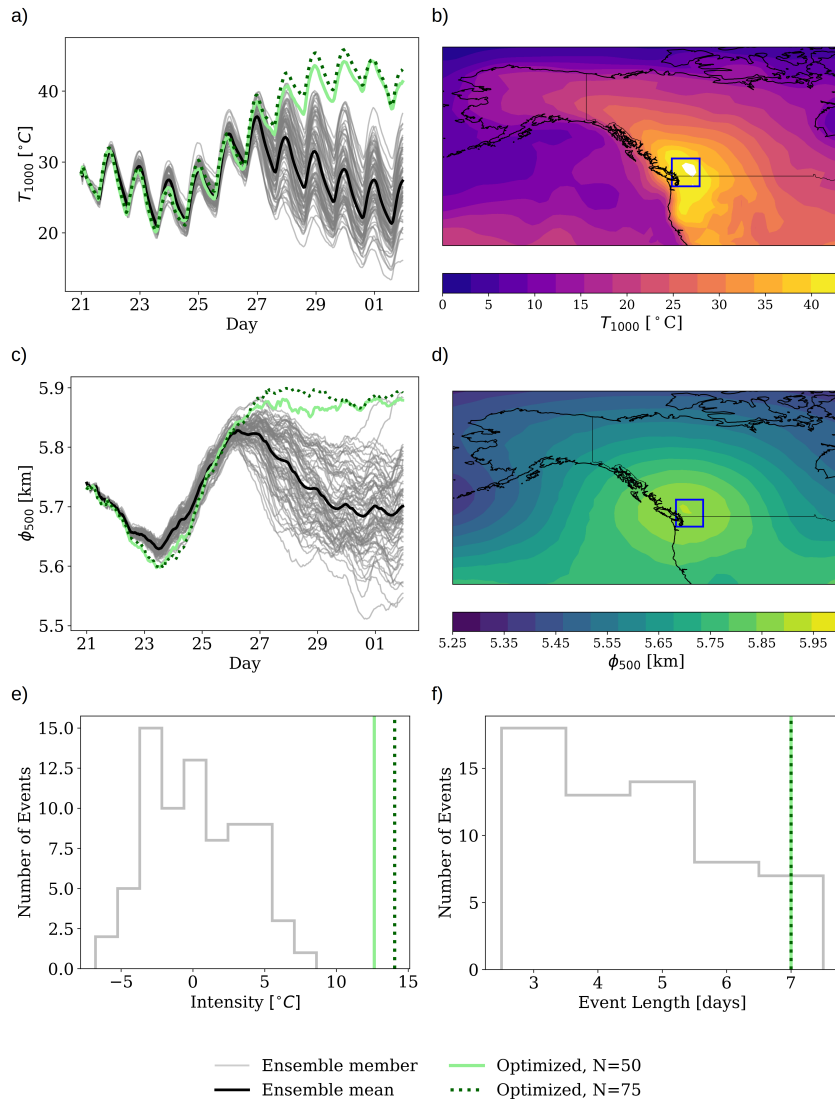


**Fig. B2** Same as Fig. 4 except with 1.4° resolution model. (a) Time series of 1000-hPa temperature for two optimized trajectories (50 and 75 steps) and a 75-member ensemble with its mean. (b) Spatial map of average temperature anomalies from the 75-step run. (c) Time series of 500-hPa geopotential height for the same set of simulations. (d) Spatial map of 500-hPa geopotential height anomalies during the event period. (e, f) Time series of heatwave intensity (defined by Eq. 4) and duration for the ensemble and optimized cases.

## References

- [1] White, R. H. *et al.* The unprecedented pacific northwest heatwave of june 2021. *Nature Communications* **14**, 727 (2023). URL <https://doi.org/10.1038/s41467-023-36289-3>.
- [2] Mass, C., Ovens, D., Christy, J. & Conrick, R. The pacific northwest heat wave of 25–30 june 2021: Synoptic/mesoscale conditions and climate perspective. *Weather and Forecasting* **39**, 275 – 291 (2024). URL <https://journals.ametsoc.org/view/journals/wefo/39/2/WAF-D-23-0154.1.xml>.
- [3] Philip, S. Y. *et al.* Rapid attribution analysis of the extraordinary heat wave on the pacific coast of the us and canada in june 2021. *Earth System Dynamics* **13**, 1689–1713 (2022). URL <https://esd.copernicus.org/articles/13/1689/2022/>.
- [4] Hazeleger, W. *et al.* Tales of future weather. *Nature Climate Change* **5**, 107–113 (2015). URL <https://doi.org/10.1038/nclimate2450>.
- [5] Shepherd, T. G. Storyline approach to the construction of regional climate change information. *Proceedings of the Royal Society A: Mathematical, Physical and Engineering Sciences* **475**, 20190013 (2019). URL <https://royalsocietypublishing.org/doi/abs/10.1098/rspa.2019.0013>.
- [6] Sillmann, J. *et al.* Event-based storylines to address climate risk. *Earth's Future* **9**, e2020EF001783 (2021). URL <https://agupubs.onlinelibrary.wiley.com/doi/abs/10.1029/2020EF001783>. E2020EF001783 2020EF001783.
- [7] Deser, C. *et al.* Insights from earth system model initial-condition large ensembles and future prospects. *Nature Climate Change* **10**, 277–286 (2020). URL <https://doi.org/10.1038/s41558-020-0731-2>.

- [8] Suarez-Gutierrez, L., Müller, W. A., Li, C. & Marotzke, J. Dynamical and thermodynamical drivers of variability in european summer heat extremes. *Climate Dynamics* **54**, 4351–4366 (2020). URL <https://doi.org/10.1007/s00382-020-05233-2>.
- [9] Maher, N., Milinski, S. & Ludwig, R. Large ensemble climate model simulations: introduction, overview, and future prospects for utilising multiple types of large ensemble. *Earth System Dynamics* **12**, 401–418 (2021). URL <https://esd.copernicus.org/articles/12/401/2021/>.
- [10] Diffenbaugh, N. S. & Davenport, F. V. On the impossibility of extreme event thresholds in the absence of global warming. *Environmental Research Letters* **16**, 115014 (2021). URL <https://dx.doi.org/10.1088/1748-9326/ac2f1a>.
- [11] Mahesh, A. *et al.* Huge ensembles part i: Design of ensemble weather forecasts using spherical fourier neural operators (2024). URL <https://arxiv.org/abs/2408.03100>. 2408.03100.
- [12] Mahesh, A. *et al.* Huge ensembles part ii: Properties of a huge ensemble of hindcasts generated with spherical fourier neural operators (2024). URL <https://arxiv.org/abs/2408.01581>. 2408.01581.
- [13] Ragone, F., Wouters, J. & Bouchet, F. Computation of extreme heat waves in climate models using a large deviation algorithm. *Proceedings of the National Academy of Sciences* **115**, 24–29 (2018). URL <https://www.pnas.org/doi/abs/10.1073/pnas.1712645115>.
- [14] Plotkin, D. A., Webber, R. J., O’Neill, M. E., Weare, J. & Abbot, D. S. Maximizing simulated tropical cyclone intensity with action minimization. *Journal of Advances in Modeling Earth Systems* **11**, 863–891 (2019). URL <https://doi.org/10.1029/2018MS001411>.

[//agupubs.onlinelibrary.wiley.com/doi/abs/10.1029/2018MS001419](https://agupubs.onlinelibrary.wiley.com/doi/abs/10.1029/2018MS001419).

- [15] Webber, R. J., Plotkin, D. A., O'Neill, M. E., Abbot, D. S. & Weare, J. Practical rare event sampling for extreme mesoscale weather. *Chaos: An Interdisciplinary Journal of Nonlinear Science* **29**, 053109 (2019). URL <https://doi.org/10.1063/1.5081461>.
- [16] Yiou, P. & Jézéquel, A. Simulation of extreme heat waves with empirical importance sampling. *Geoscientific Model Development* **13**, 763–781 (2020). URL <https://gmd.copernicus.org/articles/13/763/2020/>.
- [17] Gessner, C., Fischer, E. M., Beyerle, U. & Knutti, R. Very rare heat extremes: Quantifying and understanding using ensemble reinitialization. *Journal of Climate* **34**, 6619 – 6634 (2021). URL <https://journals.ametsoc.org/view/journals/clim/34/16/JCLI-D-20-0916.1.xml>.
- [18] Fischer, E. M. *et al.* Storylines for unprecedented heatwaves based on ensemble boosting. *Nature Communications* **14**, 4643 (2023). URL <https://doi.org/10.1038/s41467-023-40112-4>.
- [19] Ragone, F. & Bouchet, F. Rare event algorithm study of extreme warm summers and heatwaves over europe. *Geophysical Research Letters* **48**, e2020GL091197 (2021). URL <https://agupubs.onlinelibrary.wiley.com/doi/abs/10.1029/2020GL091197>. E2020GL091197 2020GL091197.
- [20] Lam, R. *et al.* Learning skillful medium-range global weather forecasting. *Science* **382**, 1416–1421 (2023). URL <https://www.science.org/doi/abs/10.1126/science.adi2336>.
- [21] Bi, K. *et al.* Accurate medium-range global weather forecasting with 3d neural networks. *Nature* **619**, 533–538 (2023). URL <https://doi.org/10.1038/>

s41586-023-06185-3.

- [22] Pathak, J. *et al.* Fourcastnet: A global data-driven high-resolution weather model using adaptive fourier neural operators (2022). URL <https://arxiv.org/abs/2202.11214>. 2202.11214.
- [23] Kurth, T. *et al.* Fourcastnet: Accelerating global high-resolution weather forecasting using adaptive fourier neural operators (2023). URL <https://doi.org/10.1145/3592979.3593412>.
- [24] Chen, L. *et al.* Fuxi: a cascade machine learning forecasting system for 15-day global weather forecast. *npj Climate and Atmospheric Science* **6**, 190 (2023). URL <https://doi.org/10.1038/s41612-023-00512-1>.
- [25] Rasp, S. *et al.* Weatherbench 2: A benchmark for the next generation of data-driven global weather models. *Journal of Advances in Modeling Earth Systems* **16**, e2023MS004019 (2024). URL <https://agupubs.onlinelibrary.wiley.com/doi/abs/10.1029/2023MS004019>. E2023MS004019 2023MS004019.
- [26] Pasche, O. C., Wider, J., Zhang, Z., Zscheischler, J. & Engelke, S. Validating deep learning weather forecast models on recent high-impact extreme events. *Artificial Intelligence for the Earth Systems* **4**, e240033 (2025). URL <https://journals.ametsoc.org/view/journals/aies/4/1/AIES-D-24-0033.1.xml>.
- [27] Ennis, K. E., Barnes, E. A., Arcodia, M. C., Fernandez, M. A. & Maloney, E. D. Turning up the heat: Assessing 2-m temperature forecast errors in ai weather prediction models during heat waves (2025). URL <https://arxiv.org/abs/2504.21195>. 2504.21195.
- [28] Kochkov, D. *et al.* Neural general circulation models for weather and climate. *Nature* (2024). URL <https://doi.org/10.1038/s41586-024-07744-y>.

- [29] Duan, S., Zhang, J., Bonfils, C. & Pallotta, G. Could neuralgcm effectively simulate future heatwaves? a case study based on the 2021 pacific northwest heatwave (2024). [2410.09120](https://doi.org/10.2410.09120).
- [30] Gelbrecht, M., White, A., Bathiany, S. & Boers, N. Differentiable programming for earth system modeling. *Geoscientific Model Development* **16**, 3123–3135 (2023). URL <https://gmd.copernicus.org/articles/16/3123/2023/>.
- [31] Materia, S. *et al.* Artificial intelligence for climate prediction of extremes: State of the art, challenges, and future perspectives. *WIREs Climate Change* **15**, e914 (2024). URL <https://wires.onlinelibrary.wiley.com/doi/abs/10.1002/wcc.914>.
- [32] Camps-Valls, G. *et al.* Artificial intelligence for modeling and understanding extreme weather and climate events. *Nature Communications* **16**, 1919 (2025). URL <https://doi.org/10.1038/s41467-025-56573-8>.
- [33] Lorenz, E. Predictability: a problem partly solved. *Seminar on Predictability, 4-8 September 1995* **1**, 1–18 (1995).
- [34] Solvik, K., Penny, S. G. & Hoyer, S. 4d-var using hessian approximation and backpropagation applied to automatically differentiable numerical and machine learning models. *Journal of Advances in Modeling Earth Systems* **17**, e2024MS004608 (2025). URL <https://agupubs.onlinelibrary.wiley.com/doi/abs/10.1029/2024MS004608>. E2024MS004608 2024MS004608.
- [35] Manshausen, P. *et al.* Generative data assimilation of sparse weather station observations at kilometer scales (2024). URL <https://arxiv.org/abs/2406.16947>. [2406.16947](https://arxiv.org/abs/2406.16947).
- [36] Vonich, P. T. & Hakim, G. J. Predictability limit of the 2021 pacific northwest heatwave from deep-learning sensitivity analysis. *Geophysical Research Letters*

- 51**, e2024GL110651 (2024). URL <https://agupubs.onlinelibrary.wiley.com/doi/abs/10.1029/2024GL110651>. E2024GL110651 2024GL110651.
- [37] Baño-Medina, J. *et al.* Are ai weather models learning atmospheric physics? a sensitivity analysis of cyclone xynthia. *npj Climate and Atmospheric Science* **8**, 92 (2025). URL <https://doi.org/10.1038/s41612-025-00949-6>.
- [38] Lucarini, V., Melinda Galfi, V., Riboldi, J. & Messori, G. Typicality of the 2021 western north america summer heatwave. *Environmental Research Letters* **18**, 015004 (2023). URL <https://dx.doi.org/10.1088/1748-9326/acab77>.
- [39] Screen, J. A. & Simmonds, I. Amplified mid-latitude planetary waves favour particular regional weather extremes. *Nature Climate Change* **4**, 704–709 (2014). URL <https://doi.org/10.1038/nclimate2271>.
- [40] Selz, T. & Craig, G. C. Can artificial intelligence-based weather prediction models simulate the butterfly effect? *Geophysical Research Letters* **50**, e2023GL105747 (2023). URL <https://agupubs.onlinelibrary.wiley.com/doi/abs/10.1029/2023GL105747>. E2023GL105747 2023GL105747.
- [41] Buehner, M. *et al.* Implementation of Deterministic Weather Forecasting Systems Based on Ensemble–Variational Data Assimilation at Environment Canada. Part I: The Global System. *Monthly Weather Review* **143**, 2532–2559 (2015). URL <http://journals.ametsoc.org/doi/10.1175/MWR-D-14-00354.1>.
- [42] Pathak, J. *et al.* Kilometer-scale convection allowing model emulation using generative diffusion modeling (2024). URL <https://arxiv.org/abs/2408.10958>. 2408.10958.
- [43] Grafke, T. & Vanden-Eijnden, E. Numerical computation of rare events via large deviation theory. *Chaos: An Interdisciplinary Journal of Nonlinear Science* **29**,

- 063118 (2019). URL <https://doi.org/10.1063/1.5084025>.
- [44] Zakine, R. & Vanden-Eijnden, E. Minimum-action method for nonequilibrium phase transitions. *Phys. Rev. X* **13**, 041044 (2023). URL <https://link.aps.org/doi/10.1103/PhysRevX.13.041044>.
- [45] Bradbury, J. *et al.* JAX: composable transformations of Python+NumPy programs (2018). URL <http://github.com/jax-ml/jax>.
- [46] DeepMind *et al.* The DeepMind JAX Ecosystem (2020). URL <http://github.com/google-deepmind>.
- [47] Hersbach, H. *et al.* The era5 global reanalysis. *Quarterly Journal of the Royal Meteorological Society* **146**, 1999–2049 (2020). URL <https://rmets.onlinelibrary.wiley.com/doi/abs/10.1002/qj.3803>.
- [48] Comeau, E., Di Luca, A. & Roberge, F. UQAM-Heatwave ERA5 Archive and Temperatures (U-HEAT) Catalog (2023). URL <https://doi.org/10.5683/SP3/Z4YOLK>.